

The Keck/DEIMOS Stellar Archive: II. Dynamical Masses and Metallicities for a Uniform Sample of Milky Way Satellites

MARLA GEHA ¹

¹*Department of Astronomy, Yale University, New Haven, CT 06520, USA*

ABSTRACT

Population-level studies of Milky Way satellites used to constrain dark matter or the threshold of galaxy formation often rely on velocity dispersions and metallicities derived from heterogeneous spectroscopic analyses. Systematic differences between data reduction pipelines and membership criteria can masquerade as astrophysical signals, or obscure real trends. Here, we present the largest self-consistent sample of spectroscopically-derived quantities for Milky Way satellite galaxies and globular clusters based on a homogeneous re-analysis of individual stars observed with the Keck/DEIMOS spectrograph. We determine enclosed dynamical masses, mean [Fe/H] metallicities, and metallicity dispersions for 67 systems with 10 or more member stars. At a given stellar mass, systems classified as satellite galaxies are well separated from globular clusters in their dynamical mass and mass-to-light ratios. The average enclosed mass densities of satellite galaxies agree with semi-analytic CDM model predictions. For satellite galaxies, we observe a break in the stellar mass-metallicity relation near $\log M_\star/M_\odot = 4$ ($M_V \sim -4.5$). Above this stellar mass, satellite galaxies show the well-known tight trend (0.16 dex scatter in [Fe/H]) of decreasing metallicity with stellar mass; below $\log M_\star/M_\odot = 4$, the mass-metallicity relation flattens and/or increases in scatter. Satellite galaxies have internal metallicity scatter between 0.3–0.4 dex across our stellar mass range. These uniform measurements will enable tighter constraints on the stellar mass-halo mass relation, improved J-factor estimates for dark matter searches, and lay a foundation for interpreting the flood of new Milky Way satellites expected in the LSST/Roman/Euclid era.

Keywords: Dwarf galaxies — Stellar kinematics — Milky Way dynamics

1. INTRODUCTION

As a system, the Milky Way’s stellar satellites provide a key snapshot of both galaxy and star cluster formation over a wide range of stellar mass. For satellite galaxies, strong correlations exist between a galaxy’s total stellar mass, dynamical/halo mass, and mean metallicity (e.g., Strigari et al. 2008; Kirby et al. 2013; Bullock & Boylan-Kolchin 2017; Simon 2019; Sales et al. 2022; Battaglia & Nipoti 2022), which differ in comparison to globular or star clusters at the same luminosity (Carretta et al. 2009; Baumgardt & Hilker 2018; Pace 2025). Both the relationship between quantities, and the scatter of systems around these scaling laws, provide insight into the formation processes of stellar systems, particularly at low stellar masses (e.g., Wetzel et al. 2016; Agertz et al. 2020; Munshi et al. 2021; Nadler et al. 2024; Ahvazi et al. 2025; Go et al. 2025; Taylor et al. 2025; Brown et al. 2025; Rey et al. 2025a).

Email: marla.geha@yale.edu

The utility of the Milky Way’s satellites depends, in part, on accurate and uniform estimates of individual stars’ kinematics and chemical abundances. These properties have been determined for millions of bright stars via measurements from the *Gaia* satellite (Gaia Collaboration et al. 2023), and ground-based wide-field spectroscopic surveys including SDSS-SEGUE (Adelman-McCarthy et al. 2008), APOGEE (Majewski et al. 2017), LAMOST (Xiang et al. 2019), and the DESI Survey (Koposov et al. 2025). Yet the limiting magnitude of current wide-field spectroscopic surveys ($r < 20$) means few stars are beyond the Milky Way Galaxy itself.

Measuring kinematics and chemistries of individual stars in the Milky Way’s satellites requires large aperture multi-object spectrographs and medium resolution spectroscopy, due to both larger distances and the higher spectral resolution needed to resolve lower dynamical masses as compared to the Milky Way. Nonetheless, the number of radial velocity measurements for stars in Milky Way satellites is rapidly growing. Many teams have contributed to the measurements of radial velocity data in Milky Way satellite galaxies (e.g., Helmi et al. 2006; Simon & Geha 2007; Battaglia et al. 2008; Li et al. 2019; Pace et al. 2020; Buttry et al. 2022; Tol-

stoy et al. 2023; Walker et al. 2023; Yang et al. 2025) and globular clusters (e.g., Baumgardt & Hilker 2018; Pace et al. 2023; Leitinger et al. 2025). The Deep Extragalactic Imaging Multi-Object Spectrograph (DEIMOS; Faber et al. 2003) on the Keck-II 10-meter telescope has contributed significantly to this effort, however, the data have been reduced and analyzed using a variety of different methods, leading to a highly heterogeneous dataset (e.g., Simon & Geha 2007; Martin et al. 2007; Geha et al. 2009; Kirby et al. 2010; Willman et al. 2011; Kim et al. 2016; Collins et al. 2017; Longeard et al. 2020; Alarcón Jara et al. 2023; Cerny et al. 2025a; Tan et al. 2025). The Keck Observatory Archive has recently opened access to over 20 years of archival DEIMOS data including hundreds of pointings towards Milky Way satellite galaxies and globular clusters.

In Geha et al. (Paper I; 2026), we describe work in which we homogeneously reduce DEIMOS multi-slit spectra and determine stellar radial velocities and equivalent width-based metallicities for over 22,000 stars in 78 Milky Way satellite systems. In this paper, we use this uniform dataset to determine integrated properties of Milky Way satellites observed with DEIMOS, including internal velocity dispersions, enclosed dynamical masses, mean metallicities and internal metallicity spreads. We then assess correlations between properties for both satellite galaxies and globular/star clusters. In § 2, we describe the DEIMOS sample and dataset. In § 3, we focus on kinematics, determining enclosed dynamical masses, mass-to-light ratios, and exploring the extent to which tidal forces from the Milky Way may be affecting our measurements. In § 4, we determine mean metallicity and internal metallicity spreads. In § 5, we combine our kinematic and metallicity measurements, with the goal of better separating satellite galaxies from star clusters, and then focus on satellite galaxies as probes of dark matter. A comparison to literature measurements and selected predictions is provided in the Appendix.

2. A HOMOGENEOUS DATASET

Paper I (Geha et al. 2026) presents a uniform analysis of individual stars in Milky Way satellites as observed with the Keck II telescope and DEIMOS spectrograph (Faber et al. 2003). This currently represents the largest sample of Milky Way satellites with homogeneously reduced kinematics and metallicities of individual stars. We include only data taken with the 1200G grating, the highest available spectral resolution with DEIMOS, which provides a resolving power of $R \sim 6000$ across a wavelength range of $6500 - 8900\text{\AA}$. As described in Paper I, multi-slit DEIMOS data spanning two decades were downloaded from the Keck Observatory Archive² (KOA). Raw data are reduced to one-dimensional

spectra using `PypeIt` which provides near Poisson statistics-level sky subtraction (Prochaska et al. 2020). Radial velocities are determined via `dmost`, a forward modeling method presented in Paper I, combining both synthetic telluric and stellar templates to determine stellar radial velocities. The precision and accuracy of these measurements and measurement errors are assessed based on thousands of independent repeat observations and comparison to larger all-sky spectroscopic surveys. The velocity error floor for the `dmost` pipeline is 1.1 km s^{-1} . The `dmost` pipeline also determines stellar metallicities ([Fe/H]) based on the Ca II triplet, with a metallicity error floor of 0.1 dex per star.

We use only data from Paper I to maintain homogeneity, avoiding possible offsets or biases when combining datasets from different telescopes (e.g., Tsantaki et al. 2022). In Figure 1, we plot the Milky Way satellites included in this work as solid symbols; open symbols are systems without archival DEIMOS coverage as compiled by Pace (2025). The majority of the solid DEIMOS points also have literature values, which we compare in Appendix A. Our velocity dispersions generally agree with literature values, but have 20-50% smaller errors (see Paper I, Figure 18). Membership probabilities (P_{mem}) are determined for individual stars in Paper I based on criteria in color-magnitude, velocity, equivalent widths, and where possible, *Gaia* DR3 parallax and proper motion measurements. We adopt a membership threshold of $P_{\text{mem}} > 0.5$. For velocity-based quantities, we additionally remove stars identified as velocity variables (the $P_{\text{mem_novar}}$ sample from Paper I). For [Fe/H]-based quantities, we remove stars fainter than $M_V > 3$ which lie outside of the empirical equivalent width-based metallicity calibration, as described in § 4.

The number of member stars per system with DEIMOS measurements varies significantly, from just 3 to over 1000 member stars (Table A1, see also Figure 16 in Paper I). There is also significant variation in radial coverage. For the majority of systems, stellar members are measured between 0.1 to 2.5 effective half-light radii ($r_{1/2}$). However, this region is entirely excluded for a handful of globular clusters due to crowding. To address variation between systems, we explicitly state the median radius of the stellar sample used for each measurement. Furthermore, we report quantities only when 10 or more member stars are measured in a given system.

Throughout this paper, we plot systems as “Satellite Galaxies” (red circles), “Globular/Star Clusters” (blue diamonds), and systems where this identification is ambiguous or “Unknown” (purple squares). We use the published classifications compiled in v1.0.6 of Pace (2025), which are based on a mix of photometric, kinematic, and metallicity information. Our analysis below confirms these classifications. Photometric quantities, including half-light radius, total luminosity, stellar mass, and distances are also taken from Pace

² <https://koa.ipac.caltech.edu>

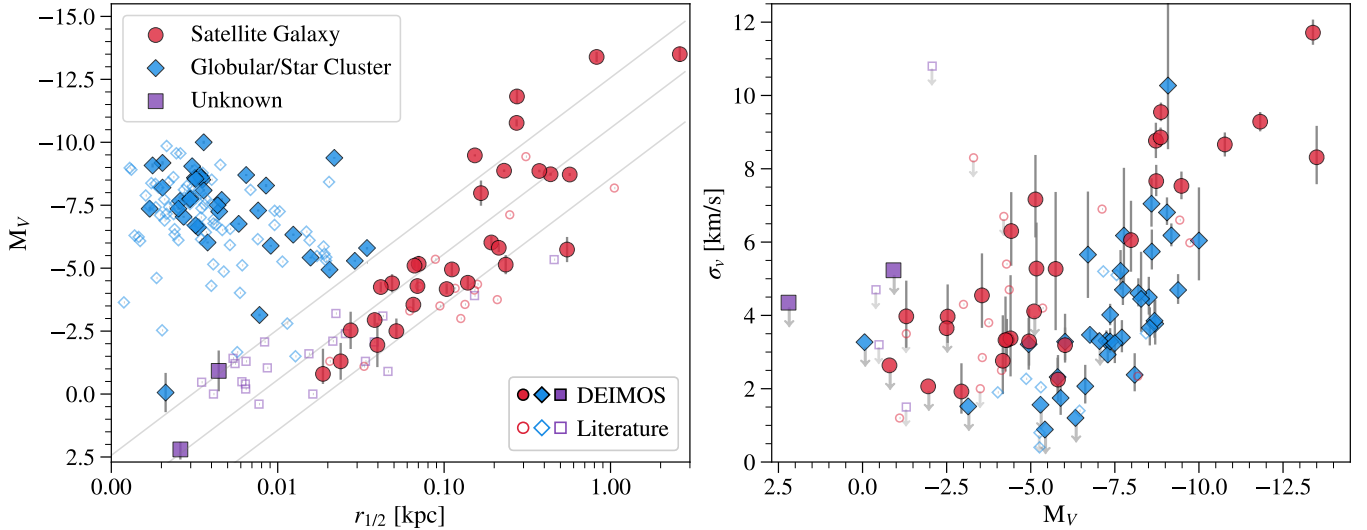


Figure 1. *Left:* Absolute magnitude (M_V) versus half-light radius ($r_{1/2}$) for confirmed Milky Way satellite galaxies (red circles), globular/star clusters (blue diamonds) and ambiguously classified objects (purple squares), as compiled in v1.0.6 of Pace (2025). Solid symbols are systems with uniform DEIMOS measurements included in this work; open symbols indicate Milky Way systems without DEIMOS coverage. Thin diagonal lines of constant effective surface brightness are shown from top to bottom: 26, 28, 30 mag arcsec $^{-2}$. *Right:* Velocity dispersion (σ_v) versus M_V as measured by this work (solid symbols), and system with non-DEIMOS literature measurements (open symbols). While the DEIMOS sample represents a fraction of all known MW systems (*left*), it includes the majority of systems with measured internal velocity dispersions (*right*).

(2025). We note that stellar mass (M_\star) is computed directly from M_V assuming a mass-to-light ratio of 2, appropriate for an old, metal-poor stellar population (Conroy & Gunn 2010).

In this work, we explore Milky Way satellites as a population, examining trends between measured properties. Shown in Figure 1, our DEIMOS sample is representative of known Milky Way satellites. The DEIMOS sample is complete for confirmed satellite galaxies with Declination $> -40^\circ$, with the exception of Antlia II and Crater II. There are 12 additional confirmed satellite galaxies in the Southern hemisphere (Declination $< -40^\circ$), and thus not visible from the Keck telescope latitude. The DEIMOS sample include less than half of known Milky Way globular clusters. A significant number of “Unknown” systems shown in Figure 1 have recent DEIMOS data which will be published in Cerny et al. (2026) using the same data reduction pipeline described in Paper I. Finally, we note that the current Milky Way satellite sample itself is likely biased against extremely low surface brightness systems ($\mu > 31$ mag arcsec $^{-2}$, left panel Figure 1). Upcoming deep imaging surveys will reveal whether or not such extreme systems exist in abundance, and to what extent this affects trends seen in the present Milky Way sample (e.g., Wheeler et al. 2025a).

3. DYNAMICAL MASS AND MASS-TO-LIGHT RATIOS

We focus first on the internal kinematics of Milky Way satellites, determining velocity dispersions based on individual stars (§ 3.1), and then calculating the enclosed dynamical mass and mass-to-light ratios (§ 3.2). We assume systems

are in dynamical equilibrium, and test the validity of this assumption by examining the enclosed mass density (§ 3.3). Imposing the membership and radial cuts described below, we present 67 Milky Way systems (29 satellite galaxies and 38 globular clusters/ambiguous systems) with DEIMOS-only kinematic measurements.

3.1. Velocity Dispersions

With the goal of a uniform comparison, we determine the internal velocity dispersion for satellite galaxies using stars enclosed within two half-light radii ($2 r_{1/2}$). This radius was chosen to maximize the number of member stars, while minimizing the risk of including unbound or foreground Milky Way stars. Since the velocity dispersions of Milky Way satellite galaxies are largely flat with radius (e.g., Walker et al. 2007; Battaglia et al. 2013), this choice does not significantly affect the resulting velocity dispersions. On the other hand, the velocity dispersions of globular clusters are a strongly decreasing function of increasing radius (e.g., Baumgardt & Hilker 2018; Sollima et al. 2019), and the radial coverage for these systems often excludes the inner half-light radius due to crowding. Thus, for globular clusters and ambiguous systems, we also attempt to measure the velocity dispersion within $2 r_{1/2}$, but extend radial coverage in cases when less than 20% of members are enclosed. For all systems, we provide the median radius of member stars used to infer the velocity dispersion (Table A1).

To minimize the presence of unresolved binary stars or other velocity-variable stars, we leverage multi-epoch mea-

surements across the full DEIMOS archive. We identify stars with variable velocities as described in Paper I, Section 5.2. Only a fraction of the full sample has multi-epoch observations (20% of member stars in satellite galaxies and 10% of globular cluster stars). Thus, there are certainly binaries present in the current sample which may affect the inferred velocity dispersions (e.g., [Minor et al. 2019](#); [Pianta et al. 2022](#); [Gration et al. 2025](#)). Paper I provides secure first epoch velocity measurements to help identify binaries and other velocity-variable stars in future spectroscopic surveys.

We calculate a system’s mean radial velocity (v_{sys}) and internal velocity dispersion (σ_v) using a two-parameter Gaussian likelihood function (Eq 7-8; [Walker et al. 2006](#)). We use the `dynesty` nested-sampling algorithm ([Speagle 2020](#)) to sample the posterior distribution, as it provides an estimate of the Bayesian evidence for each model. We adopt flat (linear) priors in velocity and velocity dispersion, but explore whether logarithmic priors over the same region in velocity dispersion space affect our results. For systems with 50 or more stars, the choice of prior does not affect the inferred velocity dispersion. For smaller samples, the choice of prior is increasingly important: for 25 stars, the adopted prior affects the resulting DEIMOS dispersions up to 0.25 km s^{-1} , while samples between 10-25 stars can differ as much as 0.75 km s^{-1} . A more thorough exploration on the choice of priors will be presented a future paper. Here, we adopt a linear prior which produces more conservative (larger) upper limits in the limit of small sample size. Nonetheless, in Paper I, we showed that these DEIMOS-derived velocity dispersions generally agree with literature values to within 1σ , but are more precise with 20-50% smaller errors (see Figure 18 of Paper I).

In order to determine whether a system’s internal velocity dispersion is resolved by the DEIMOS velocity sample, we compare the Bayesian evidence between our two-parameter Gaussian likelihood to a Gaussian model with zero internal dispersion (e.g., the observed velocity dispersion is due to measurement errors only). Following recommended thresholds from [Kass & Raftery \(1995\)](#), we consider the velocity dispersion as resolved (non-zero) if the log of the ratio of evidences is larger than unity. If resolved, we quote the 1-sigma errors (16th–84th percentile range) of the posterior distributions. In cases when the dispersion is not resolved, we report only an upper limit on the velocity dispersion as the 95th percentile of the posterior distribution.

In the right panel of Figure 1, we show the measured velocity dispersion versus absolute magnitude (σ_v vs. M_V). Systems in which the velocity dispersion is resolved are plotted with 1-sigma error bars, while systems with unresolved dispersions are plotted with downward errors at the location of the 95% upper confidence limit. 12 of 67 systems have unresolved velocity dispersions in the DEIMOS sample (see

Table 1). The smallest resolved velocity dispersion is the globular cluster NGC 7492 ($\sigma_v = 1.7^{+0.5}_{-0.4} \text{ km s}^{-1}$, 21 stars), while the strongest upper limit is the globular cluster Eridanus ($\sigma_v < 0.9 \text{ km s}^{-1}$, 24 stars). For both satellites galaxies and star clusters in Figure 1, velocity dispersions loosely decrease with luminosity. In § 5.2, we further explore the velocity dispersions of satellite galaxies, focusing on trends with stellar mass and half-light radius as constraints on dark matter models.

3.2. Enclosed Dynamical Mass and M/L

Given the wide range of physical properties in our sample, we opt for a simple estimate of the enclosed dynamical mass. We defer more detailed mass modeling (e.g., [Read et al. 2021](#); [Guerra et al. 2023](#); [Bañares-Hernández et al. 2025](#)) to future work.

[Wolf et al. \(2010\)](#) showed that the dynamical mass enclosed within the half-light radius of a dispersion-supported system is robustly determined with only mild assumptions about the orbital anisotropy of its constituent stars. We determine the dynamical mass according to [Wolf et al. \(2010\)](#) as: $M_{1/2} = 4\sigma_v^2 r_{1/2}/G$, combining our DEIMOS velocity dispersions (σ_v) with the half-light radius ($r_{1/2}$) from the literature compilation of [Pace \(2025\)](#). We compute errors on $M_{1/2}$ by Monte Carlo sampling errors in velocity dispersion and half-light radius.

In the left panel of Figure 2, we plot the dynamical mass as a function of stellar mass, $M_{1/2}$ vs. M_\star . There is a general trend of decreasing dynamical mass with decreasing stellar mass for both globular clusters and satellite galaxies. However as expected, satellite galaxies have significantly larger dynamical mass at a given stellar mass. The DEIMOS spectral resolution limits the minimum measured dynamical mass above $\log[M_{1/2}/M_\odot] \sim 4$.

In the right panel of Figure 2, we plot the enclosed mass-to-light ratio ($M_{1/2}/L_{1/2}$) as a function of stellar mass, where $L_{1/2}$ is half the total V -band luminosity. For globular clusters, we expect $M_{1/2}/L_{1/2} = 1.5–3$, consistent with baryonic-only old stellar populations ([Conroy & Gunn 2010](#)). There is one globular cluster, Sgr II ($\log M_\star/M_\odot = 4.5$, $M_{1/2}/L_{1/2} = 19 \pm 8$), which appears to lie between the globular cluster and satellite galaxy population. Our velocity dispersion for Sgr II of $2.3 \pm 0.5 \text{ km s}^{-1}$ (34 stars) is slightly larger than that of [Longeard et al. \(2021\)](#), $1.7 \pm 0.5 \text{ km s}^{-1}$ (47 stars), based on VLT FLAMES data. Both samples suggest a very small metallicity dispersion, and we thus maintain that this object is correctly classified as a star cluster (see also [Zaremba et al. 2025](#)). While a handful of globular clusters have large upper $M_{1/2}/L_{1/2}$ limits, these are all faint systems ($\log M_\star/M_\odot < 4.5$), whose expected velocity dispersions are below the DEIMOS velocity uncertainty floor. Nonetheless, the median resolved mass-to-light ratio for all DEIMOS

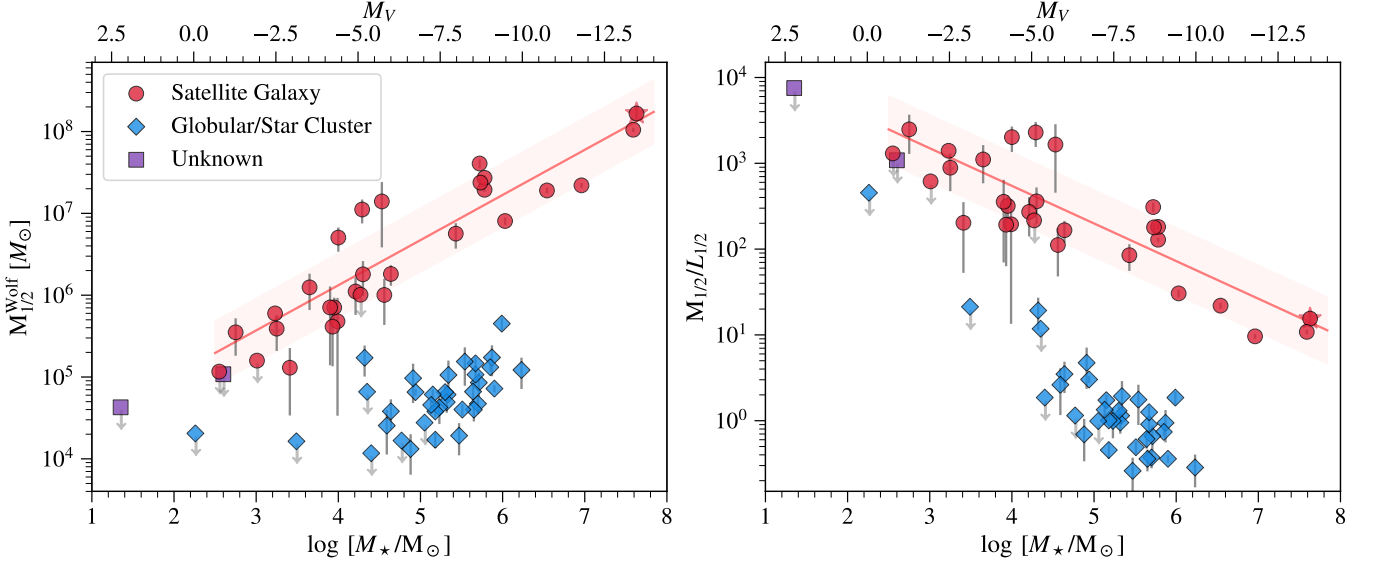


Figure 2. *Left:* Dynamical mass enclosed within the half-light radius ($M_{1/2}$) versus stellar mass ($\log M_\star$). *Right:* Mass-to-light ratio ($M_{1/2}/L_{1/2}$) versus stellar mass. In both panels, the top x-axis shows absolute magnitude (M_V). At a given stellar mass, satellite galaxies (red circles) have larger dynamical mass and higher mass-to-light ratios compared to globular clusters (blue diamonds). Globular clusters are consistent with baryonic-only mass. Satellite galaxies show decreasing enclosed dynamical mass and increasing $M_{1/2}/L_{1/2}$ with decreasing stellar mass.

globular clusters is $M_{1/2}/L_{1/2} = 1.0$. This is slightly lower than predicted for a baryon-only system because we are determining the average velocity dispersions enclosed within $2r_{1/2}$, rather than fitting a model to the velocity dispersion profile.

On the other hand, for satellite galaxies in Figure 2, the mass-to-light ratio clearly increases with decreasing stellar mass. For luminous satellite galaxies ($\log M_\star/M_\odot > 6$), mass-to-light ratios are well in excess of the stellar mass alone: $M_{1/2}/L_{1/2} \sim 10 - 30$, with a minimum value for Leo I of $M_{1/2}/L_{1/2} = 10 \pm 1$. For the least luminous satellite galaxies ($\log M_\star/M_\odot < 5$) mass-to-light ratios rise above 1000, with a maximum value for Segue 1 of $M_{1/2}/L_{1/2} \sim 2500 \pm 1200$. In both panels of Figure 2, we fit a linear function for satellite galaxies only. We include only systems with resolved velocity dispersions, showing the best-fit model and rms scatter in the y-direction. We first fit the dynamical masses versus stellar mass, finding $M_{1/2} = 0.54^{+0.07}_{-0.03} \log M_\star + 3.89^{+0.27}_{-0.29}$. The slope of this relationship is in good agreement with predicted slope of 0.55 from the GRUMPY semi-analytical model of galaxy formation applied to the Caterpillar dark matter-only simulations (Eq. 8; Kravtsov & Wu 2023), which we overplot in Figure A1 and discuss further in § 5.2.

In the right panel of Figure 2, we also fit a linear model to $M_{1/2}/L_{1/2}$ vs. $\log M_\star$, again only for satellite galaxies with resolved velocity dispersions. Recent numerical simulations suggest a minimum stellar mass for galaxy formation, and that extremely low stellar mass systems are hosted by a wide range of dark matter halo masses (e.g., the stellar mass-halo

mass relationship has a large scatter). Suggested stellar mass thresholds for galaxy formation range from a thousand (Taylor et al. 2025; Brown et al. 2025) to a few hundred (Munshi et al. 2021; Wheeler et al. 2025b) solar masses. However, these prediction remain highly dependent on differences in baryonic physics prescriptions such as gas heating/cooling physics, reionization, and molecular hydrogen cooling models (e.g., Nadler 2025). We note a lack of extremely high mass-to-light ratio systems at the faintest end of this relationship ($\log M_\star/M_\odot < 3.5$, $M_{1/2}/L_{1/2} > 2500$) which would be easily detected if present. While the lack of high M/L systems might imply that the scatter in the stellar mass-halo mass relation does not significantly increase at extremely low stellar masses (Nadler et al. 2020; Danieli et al. 2023), there are also a number of systems with $M_{1/2}/L_{1/2}$ upper limits. If the true $M_{1/2}/L_{1/2}$ of these unresolved systems are significantly smaller than current limits, this would increase scatter below $\log M_\star/M_\odot < 3.5$ as compared to more luminous Milky Way satellite galaxies. Resolving this issue requires larger samples of individual stars with higher spectral resolution than possible with the Keck/DEIMOS spectrograph.

3.3. Enclosed Density and Tidal Influence on Milky Way Satellites

The analysis above implicitly assumes that Milky Way satellites are in dynamical equilibrium. We next examine orbital parameters to assess the degree to which Milky Way tidal forces may be affecting our measured quantities. All of our satellite systems have proper motions measured by *Gaia* DR3, although in many cases this is based on very few stars. We determine orbital parameters based on the proper

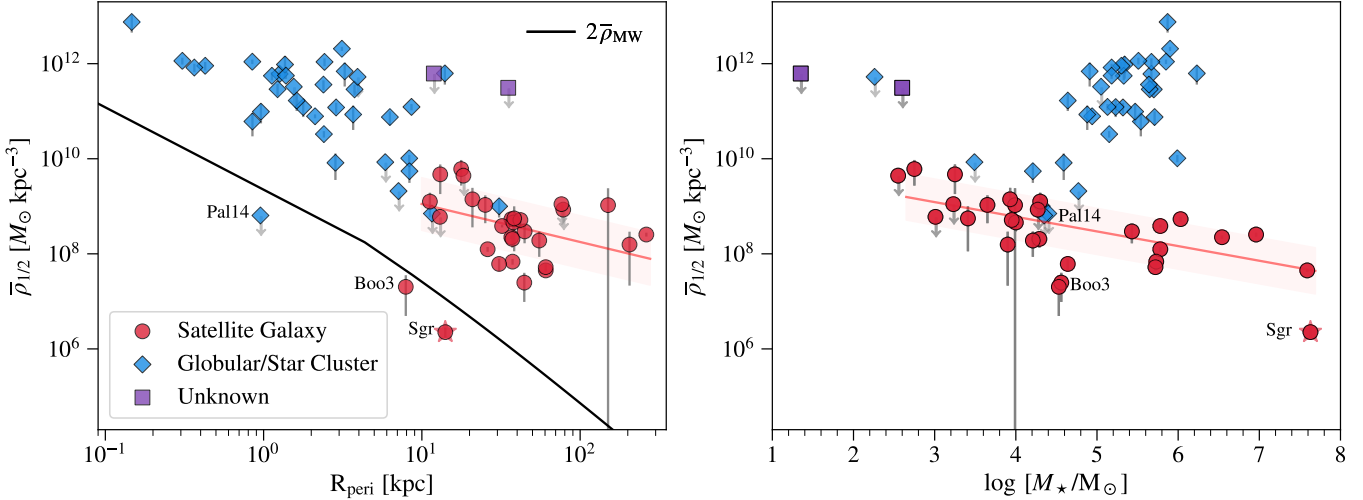


Figure 3. *Left:* The average enclosed mass density ($\bar{\rho}_{1/2}$) plotted against orbital pericenter (R_{peri}). The black line represents twice the enclosed Milky Way density as a function of radius ($2\bar{\rho}_{\text{MW}}$). Systems near this line are expected to show signs of tidal disruption. While most systems are far from this threshold, we label systems close to the disruption line. *Right:* We plot $\bar{\rho}_{1/2}$ against total stellar mass. For satellite galaxies, lower luminosity systems tend to have higher enclosed mass density.

motion and distance as compiled by [Pace \(2025\)](#), and the DEIMOS radial velocity. We use the `galpy` orbit integration software ([Bovy 2015](#)) and `MWPotential2014` for the gravitational potential of the Milky Way, which is static in time and does not include the impact of the LMC. As suggested by [Bovy \(2015\)](#), we adopt a 50% larger dark matter halo mass ($1.2 \times 10^{12} M_\odot$) than the `MWPotential2014` default.

To assess whether a system is vulnerable to gravitational disruption, we follow [Pace et al. \(2022\)](#) by comparing the average enclosed density ($\bar{\rho}_{1/2}$) of each system to twice the enclosed Milky Way density ($\bar{\rho}_{\text{MW}}$) at the same pericentric distance. If a satellite sits below this line, its Jacobi tidal radius is larger than the half-light radius and it will likely be tidal disrupting. In Figure 3 (right panel), the majority of Milky Way satellite galaxies and globular clusters lie well above this threshold. We label two satellite galaxies which sit close to this threshold: the disrupting satellite galaxy Sgr dSph ([Majewski et al. 2003](#)), and Boötes III which has long been suspected to be tidally disrupting ([Carlin & Sand 2018; Pace et al. 2022](#)).

One globular cluster in Figure 3 lies near the tidal-disruption threshold. Palomar 14 is an outer halo system, and is previously known to have a low stellar density ([Zonoozi et al. 2011](#)). While it is currently at a heliocentric distance of 74 kpc and near apocenter, its orbital properties suggest a plunging orbit, with pericenter of less than 1 kpc ([Baumgardt et al. 2019; Zonoozi et al. 2024](#)).

We first focus on globular clusters as a population in Figure 3. Globular clusters with the highest stellar densities ($\bar{\rho}_{1/2}$) are also the most massive systems with the smallest pericentric radii. Globular clusters with lower stellar densities tend to have lower stellar mass and orbit in the

outer Galactic halo. Splitting the globular cluster sample at $\bar{\rho}_{1/2} = 10^{10} M_\odot \text{ kpc}^{-3}$, lower density clusters have a mean current distance (pericenter) of 37 kpc (14 kpc), compared to 16 kpc (3 kpc) for higher density globular clusters. This can be understood as lower density clusters will not survive close passage near the Galactic plane, while more massive globular clusters are preferentially removed from the outer halo via dynamical friction (e.g., [Gnedin & Ostriker 1997](#)).

We next examine trends for satellite galaxies in Figure 3. The average mass density, $\bar{\rho}_{1/2}$, mildly increases with both decreasing pericentric distance and decreasing stellar mass. We again fit a linear model to satellite galaxies only, first removing the two disrupting satellites and satellites in which the velocity dispersion is unresolved. We report the coefficients of these fits in the Appendix. [Kaplinghat et al. \(2019\)](#) first pointed out a trend of increasing $\bar{\rho}$, enclosed within a fixed 150 pc, with decreasing pericenter for classical Milky Way satellites, suggesting that only dense satellite galaxies can survive small pericenters. While we see a similar trend for $\bar{\rho}_{1/2}$ versus R_{peri} , the slope is just 2σ from a flat relation. Interestingly, [Pace et al.](#) (see their Figure 5; [2022](#)) sees significantly more scatter between $\bar{\rho}_{1/2}$ and R_{peri} , regardless of whether the LMC is included in the orbit integration. Finally, it is curious that the minimum $\bar{\rho}_{1/2}$ values for both the satellite galaxy and globular cluster populations follow one magnitude above the Milky Way tidal threshold.

In the right panel of Figure 3, the relationship for satellite galaxies between $\bar{\rho}_{1/2}$ and stellar mass is perhaps easier to interpret. As noted by [Kravtsov & Wu \(2023\)](#), if galaxies of larger stellar mass form in higher-mass Cold Dark Matter (CDM) halos on average, but $r_{1/2}$ is roughly a fixed fraction of the virial radius, then larger stellar masses systems

are predicted to have lower $\bar{r}_{1/2}$. The observed trend suggests that lower stellar mass satellites, on average, are hosted in lower mass dark matter halos even at the extremely low stellar masses. However, the large number of upper limits in density/velocity dispersion at the lowest stellar mass end may reduce or erase this trend when improved measurements are available. We discuss this trend further in § 5.2.

4. METALLICITY

We next investigate the mean metallicity ($\overline{[\text{Fe}/\text{H}]}$) and internal metallicity spread ($\sigma_{[\text{Fe}/\text{H}]}$) in our Milky Way satellite sample. In Paper I, we measured the combined equivalent widths of the Ca II triplet (CaT) lines (8498.0, 8542.1 and 8662.1 Å) and determined stellar metallicities, $[\text{Fe}/\text{H}]$, for individual stars based on the CaT-[Fe/H] calibration of Navabi et al. (2026). This calibration is an update to Carrera et al. (2013), using the same functional form, with improved agreement with full spectrum-fitting results at the higher metallicity end ($[\text{Fe}/\text{H}] > -1.5$). This empirical calibration is valid only for red giant branch stars, $M_V < 3$ (see Paper I, Figure 13), and we thus remove horizontal branch stars and intrinsically fainter stars for this analysis. These CaT-based $[\text{Fe}/\text{H}]$ allow for homogeneous metallicity estimates across a wide range of signal-to-noise. We again enforce a minimum number of 10 stars per system when determining metallicity spreads (55 systems), but relax this criteria to a minimum of 7 stars (61 systems) when determining the mean metallicity.

To determine the mean metallicity, $\overline{[\text{Fe}/\text{H}]}$, and internal metallicity spread, $\sigma_{[\text{Fe}/\text{H}]}$, in each system, we assume the same two-parameter Gaussian model as detailed in § 3.1, in which the individual metallicity measurements and associated errors are described by a mean metallicity and internal metallicity spread. We also use the same sampling algorithm, assuming flat priors, and test if the metallicity spread is resolved (non-zero) if the log of the ratio of Bayesian evidences is larger than unity. Metallicities are again determined inside of $2 r_{1/2}$ to maintain uniformity, but are extended for globular clusters to a maximum of $4 r_{1/2}$ in cases where there are less than 10 available member stars. We provide $\overline{[\text{Fe}/\text{H}]}$, $\sigma_{[\text{Fe}/\text{H}]}$, and associated errors for individual Milky Way systems in Table A1.

4.1. The Stellar Mass-Metallicity Relation

The stellar mass-metallicity relationship is a fundamental scaling relation in galaxy evolution (e.g., Gallazzi et al. 2005; Kirby et al. 2011; Simon 2019; Bose & Deason 2025). The slope and scatter of this relation provides insights into the balance between pristine gas inflow and metal-enriched outflows driven by stellar feedback. The tight observed scatter in this relationship (~ 0.2 dex) has historically been used to argue against significant tidal disruption for Milky Way satellites (Simon & Geha 2007; Kirby et al. 2013), however, Riley et al. (2025) demonstrated that significant tidal disruption

may not increase scatter in the mass-metallicity relationship, but rather lead to a shallower slope.

In the left panel of Figure 4, we plot stellar metallicity versus stellar mass ($\overline{[\text{Fe}/\text{H}]}$ vs. M_\star). We first focus on globular clusters which show no trend in this panel. Our DEIMOS Milky Way globular cluster sample shows the well-known apparent metallicity floor (Harris 2010), such that no clusters lie below $\overline{[\text{Fe}/\text{H}]} < -2.36$. In the larger Milky Way sample of globular clusters, only one system is known at slightly lower metallicity, ESO 280-SC06, at $\overline{[\text{Fe}/\text{H}]} < -2.54$ (Usman et al. 2025). In stark contrast, eight of our satellite galaxies have $\overline{[\text{Fe}/\text{H}]} < -2.5$, and the majority of satellite galaxies are more metal-poor than our most metal-poor globular cluster, NGC 6341 (M 92) with $\overline{[\text{Fe}/\text{H}]} = -2.35 \pm 0.02$. The most metal-poor satellite galaxies in our sample is Eri IV with $\overline{[\text{Fe}/\text{H}]} = -2.93 \pm 0.09$, consistent with Heiger et al. (2024). The most metal-poor Milky Way satellite galaxy currently published is Pictor II with $\overline{[\text{Fe}/\text{H}]} = -2.99 \pm 0.06$ (Pace et al. 2025).

Satellite galaxies show a tight trend of decreasing metallicity with stellar mass down to $\log M_\star/M_\odot = 4$ ($M_V \sim -4.5$). We first fit a linear model to satellite galaxies between $4 < \log M_\star/M_\odot < 8$ (16 systems), excluding the currently disrupting Sgr dSph (red star symbol in Figure 4). As described and reported in the Appendix, we find a fit of $\overline{[\text{Fe}/\text{H}]} = 0.33^{+0.04}_{-0.04} \log[M_\star] - 3.98^{+0.22}_{-0.21}$. The average scatter in the intercept of this fit is 0.22 dex. We also compute scatter as the root-mean-square, finding a scatter of 0.16 dex above $\log M_\star/M_\odot > 4$. Compared to Kirby et al. (2013) and Simon (2019), our slope is slightly steeper (0.33 ± 0.04 vs. 0.29 ± 0.02) with similar scatter. See the Appendix for further comparison to previous results.

The behavior of the mass-metallicity relationship changes significantly at $\log M_\star/M_\odot \approx 4$ ($M_V \sim -4.5$). Below this stellar mass, the trend becomes more shallow and/or increases in scatter (Figure 4, left panel). A flattening of the mass-metallicity relationship for extremely low stellar mass galaxies has been previously noted. However, Fu et al. (2023) suggest a higher stellar mass transition of $\log M_\star/M_\odot \sim 5$ ($M_V > -7.0$) based on narrow-band photometric *HST* metallicities, while previous spectroscopic measurements suggest only an increase of scatter below $\log M_\star/M_\odot \sim 4$ (Simon 2019; Pace 2025). Again, see the Appendix for a comparison to previous results.

A stellar mass threshold below which the mass-metallicity relation changes is also seen in theoretical models of galaxy formation, but its value and interpretation remain uncertain. Earlier cosmological baryonic zoom-in simulations of isolated low-mass galaxies struggled to systematically recover the level of metal enrichment for galaxies with $\log M_\star/M_\odot \lesssim 5$, finding that these systems are especially sensitive to choices of star formation and stellar feedback prescriptions,

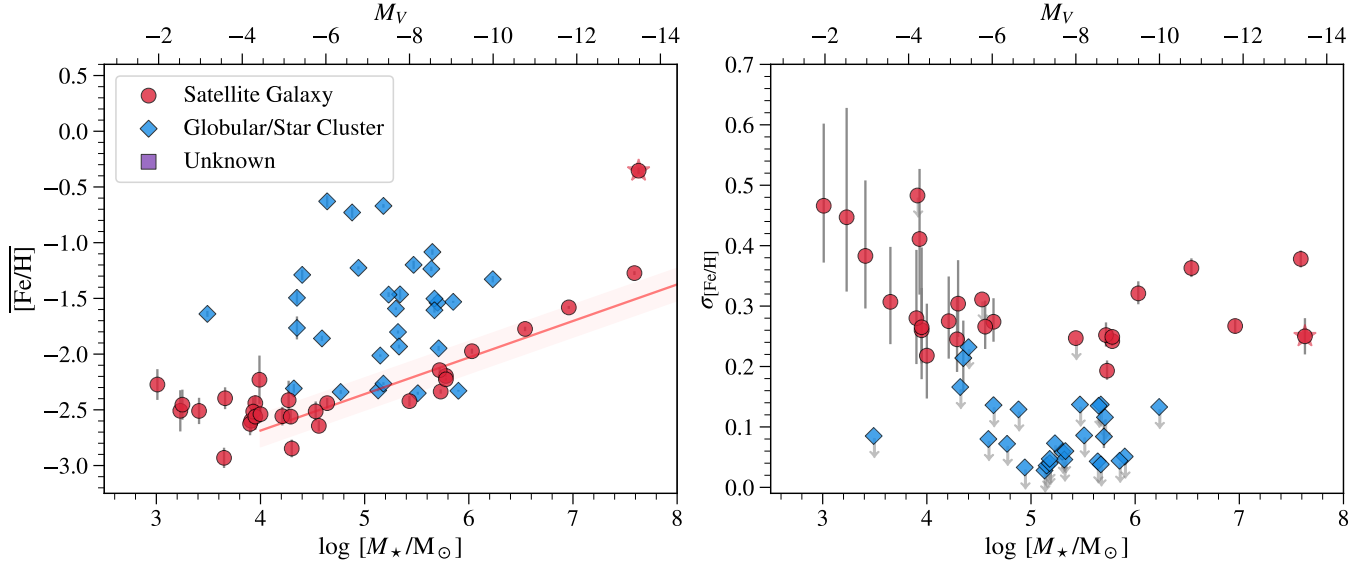


Figure 4. *Left:* The mean stellar metallicity ($\langle \text{[Fe/H]} \rangle$) and (*right*) the internal metallicity spread ($\sigma_{\text{[Fe/H]}}$) versus total stellar mass. Systems are color-coded as previous figures. Satellite galaxies show the well-known mass-metallicity relationship down to $\log [M_\star / M_\odot] \approx 4$. Below this stellar mass threshold, the mass-metallicity relationship for satellite galaxies flattens and/or increases scatter. The internal metallicity scatter shows a similar upturn or increased scatter at this stellar mass. The red star symbol at $\log [M_\star / M_\odot] \approx 7.6$ is the disrupting Sagittarius dSph which we do not include in our fits. In contrast, globular clusters show no mass-metallicity relation and have internal metallicity dispersions below 0.2 dex.

nucleosynthetic yields, and Population III modeling (e.g., Macciò et al. 2017; Wheeler et al. 2019; Agertz et al. 2020; Gandhi et al. 2022). However, both recent cosmological zoom-in simulations and semi-analytic models of low-mass galaxies in Milky Way-like environments show metal enrichment closer to observed Milky Way satellites, and suggest a flattening in the mass-metallicity relation between $\log M_\star / M_\odot < 4 - 5$ is due to either Population III IGM enrichment and enrichment from the host MW-mass system (Ahvazi et al. 2025; Rey et al. 2025b) or choices of feedback prescriptions that affect galactic winds and metal loss/retention from the low-mass galaxies (Manwadkar & Kravtsov 2022; Rey et al. 2025a), although stochastic sampling may also play a role (Go et al. 2025; Andersson et al. 2025). See the Appendix for a direct comparison to selected predictions.

4.2. Metallicity Spreads

The presence of an internal metallicity spread is a key test in discerning between star clusters and galaxies (Willman & Strader 2012). The underlying assumption is that dark matter-dominated galaxies better retain enriched ejecta from stellar feedback and form further generations of stars, increasing the metallicity differences between individual stars in a given system. While globular clusters are now recognized to also host significant internal abundance spreads for light elements (Bastian & Lardo 2018), the spread in overall metallicity is significantly smaller as compared to galax-

ies, with spectroscopic studies suggesting of order $\sigma_{\text{[Fe/H]}} \sim 0.05$ dex (Carretta et al. 2009; Latour et al. 2025).

In the right panel of Figure 4, we plot the internal metallicity spread versus stellar mass ($\sigma_{\text{[Fe/H]}}$ vs. M_\star). Nearly all globular clusters show unresolved metallicity spreads with a median 95% upper limit of $\sigma_{\text{[Fe/H]}} < 0.07$ dex. We do not plot one globular cluster which has a significant resolved metallicity dispersion: NGC 2419. NGC 2419 has $\sigma_{\text{[Fe/H]}} = 0.19$ dex, consistent with the prior CaT measurement by Cohen et al. (2010). However, Larsen et al. (2019) interprets the CaT spread as an indicator of a spread in alpha-elements rather than iron; the true iron abundance dispersion of NGC 2419 is likely much smaller (Bailin 2019).

In contrast to globular clusters, the internal metallicity dispersion of satellite galaxies are 0.2 dex and larger. We determine the metallicity spread within 2 half-light radius and do not remove metallicity gradients which are present for the most luminous satellite galaxies ($\log M_\star / M_\odot > 6$). For bright systems such as the Fornax and Sgr dSph, this choice increases our values over the literature (see Appendix), however, we believe this is a more fair comparison when including the faintest Milky Way systems for which there are too few stars to measure gradients. The median metallicity spread of the full Milky Way DEIMOS satellite galaxy sample is $\sigma_{\text{[Fe/H]}} = 0.27$ dex. The scatter in $\sigma_{\text{[Fe/H]}}$ is significant with systems ranging from 0.2-0.5 dex. The range in scatter is smaller than both previous measurements (see Appendix) and predictions from cosmological zoom-in simulations (Escala et al. 2018; Taylor et al. 2025; Go et al. 2025). At the

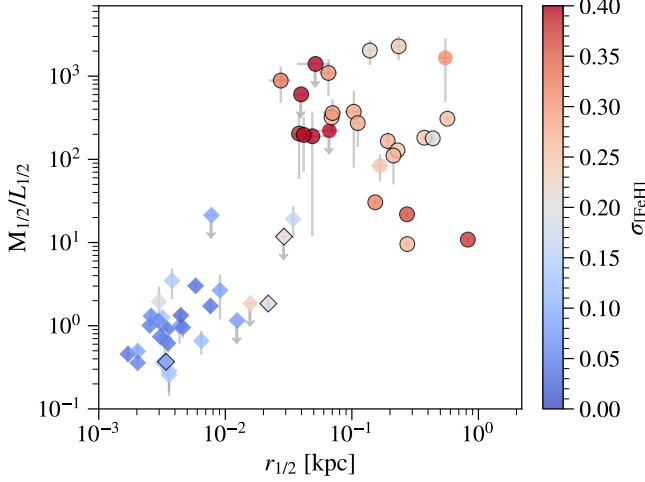


Figure 5. Combining kinematic and metallicity measurements, we plot the mass-to-light ratio ($M_{1/2}/L_{1/2}$) versus the half-light radius ($r_{1/2}$). Symbols are color-coded based on their internal metallicity dispersion ($\sigma_{[\text{Fe}/\text{H}]}$). Systems with resolved metallicity dispersions are shown with black outlines. Satellite galaxies (circles) and star clusters (diamonds) are well separated in these properties.

lowest stellar mass ($\log M_{\star}/M_{\odot} < 3.8$), $\sigma_{[\text{Fe}/\text{H}]}$ appears to increase, however, these systems have large errors due to a small sample size (15 or fewer stars).

5. DISCUSSION

We combine our kinematic and metallicity measurements, with the goal of better separating satellite galaxies from star clusters (§ 5.1), and then consider satellite galaxies as probes of dark matter (§ 5.2).

5.1. Separating Galaxies and Star Clusters

Cleanly separating satellite galaxies from globular clusters is particularly challenging for the Milky Way’s faintest systems ($M_V > -4$). Yet a clean census is critical to understanding how both populations formed (e.g., Baumgardt et al. 2022; Simon et al. 2024; Smith et al. 2024; Cerny et al. 2025b). Given limited and heterogeneous data, there is no one way to classify systems. Various indicators, or combination of indicators, are currently used including M_V , $r_{1/2}$, $\sigma_{[\text{Fe}/\text{H}]}$, and stellar mass segregation.

In Figure 5, we combine kinematic and photometric properties, plotting the mass-to-light ratio versus half-light radius ($M_{1/2}/L_{1/2}$ vs. $r_{1/2}$), color-coding by the internal metallicity spread ($\sigma_{[\text{Fe}/\text{H}]}$). Systems in which the metallicity spread is resolved are outlined in black. While this figure is not optimized for classification, it serves as a relatively clean separation between globular clusters and satellite galaxies. We have already commented on one system, Sgr II, which does not separate fully (the blue diamond with $r_{1/2} = 0.03$ kpc). Figure 5 demonstrates that while size alone remains a useful indicator of classification, there is overlap in the region

between $r_{1/2} = 25 - 40$ pc, and the addition of spectroscopic measurements (e.g., mass-to-light ratio and metallicity spread) significantly improves separation. Nonetheless, recent predictions suggest a population of extremely low mass galaxies which would overlap even in this space with star clusters (e.g., Errani et al. 2024; Taylor et al. 2025).

5.2. Satellite Galaxies: Dark Matter tests

The observed properties of extremely low mass galaxies provide strong constraint on the nature of dark matter (e.g., Bullock & Boylan-Kolchin 2017; Sales et al. 2022; Cruz et al. 2025; May et al. 2025; Delos et al. 2025). Rather than constrain any particular dark matter model, here we aim to provide robust observed relationships which can be used to constrain a wide range of dark matter model predictions.

In the left panel of Figure 6, we plot our DEIMOS-derived velocity dispersions versus half-light radius (σ_v vs. $r_{1/2}$) for satellite galaxies only. Under the assumption that the each system represents a dark matter halo in CDM, the distribution of these points constrains the range of total halo mass and concentration for the Milky Way satellite galaxy population. For example, Esteban et al. (2024) showed that the scatter in σ_v vs. $r_{1/2}$ is consistent with expectations from CDM (dashed region, left panel Figure 6), with outliers to larger sizes and lower velocity dispersions being explained by tidal stripping (dotted region), similar to results from Errani et al. (2022). We note that the observed σ_v vs. $r_{1/2}$ outliers in Figure 6, include the Hercules, Boötes I and Boötes III dSphs, all of which are suspected of tidal disruption (Ou et al. 2024; Sandford et al. 2025; Carlin & Sand 2018). We again fit a linear model to these data, providing the fit parameters in the Appendix.

In the right panel of Figure 6, we plot velocity dispersion against stellar mass (σ_v vs. M_{\star}). While these data are roughly linear, there is significant scatter, particularly below $\log M_{\star}/M_{\odot} < 4.5$. The distribution is marginally consistent with the semi-analytic predictions from Ahvazi et al. (2025) in both slope and scatter. Combining σ_v and $r_{1/2}$, we plot the enclosed mass density, $\bar{\rho}_{1/2}$, in the right panel of Figure 3. As discussed in § 3.3, the overall trend of increasing mass density with decreasing stellar mass is understood if galaxies of larger stellar mass form in higher-mass halos on average, and the fact that the half-light radius is a fixed fraction of the virial radius with some scatter (Kravtsov 2013; Kravtsov & Wu 2023).

Finally, the Milky Way satellites remain attractive sites to search for signals of dark matter annihilation and decay at gamma-ray wavelengths (e.g., Abdo et al. 2010; Strigari 2018). The strength of these signals depend on details of the dark matter particle itself and the combined central dark matter density and heliocentric distance of a given satellite galaxy. The latter is often parameterized by the ‘J-factor’.

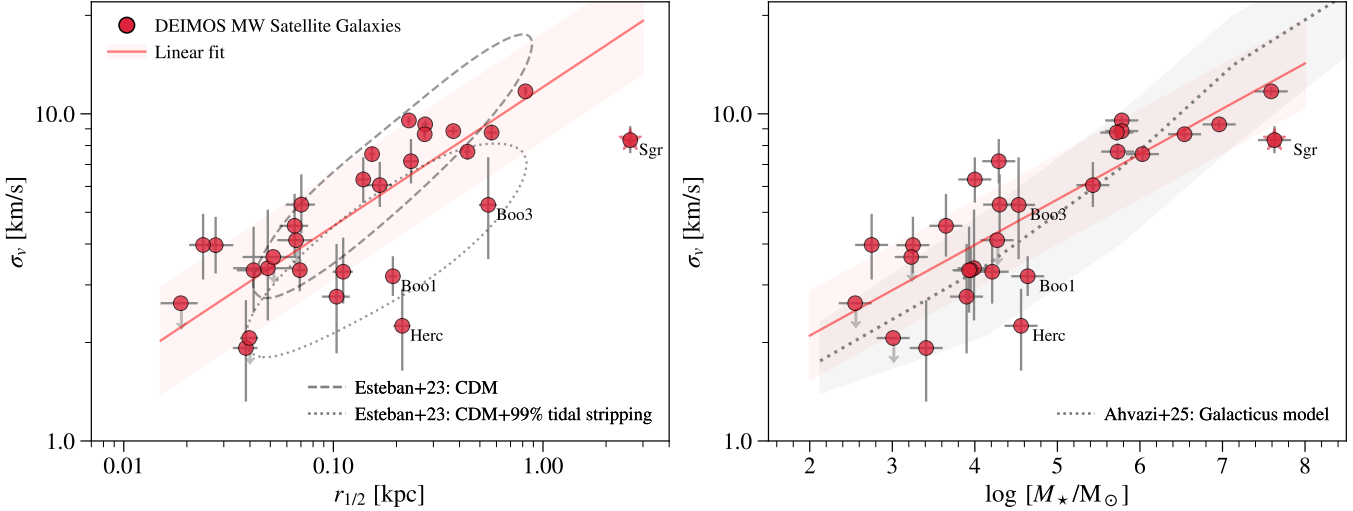


Figure 6. *Left:* The velocity dispersion versus half-light radius (σ_v vs. $r_{1/2}$) for the DEIMOS satellite galaxies only. The red line is a linear fit to the data, exclude the disrupting Sgr system (star symbol). The dashed region is the 68% enclosed region for a representative population of Milky Way-like satellites residing in CDM halos (Esteban et al. 2024). The dotted region is the same model with 99% tidal stripping. *Right:* The velocity dispersion plotted versus stellar mass (σ_v vs. M_\star). This agrees well with prediction from the semi-analytic model from Ahvazi et al. (2025). Values for the linear fits (red lines) are provided in the Appendix.

Using the scaling relations from Pace & Strigari (2019), our highest J-factor systems is Segue 1, $\log_{10} J [\text{GeV}^2 \text{cm}^{-5}] = 19.4 \pm 0.4$. This object is also among the highest ranked systems in McDaniel et al. (2024), however, because J-factors scale as velocity dispersion to the fourth power, our reduced velocity dispersion errors translates into smaller J-factor errors. Meaningful constraints on the dark matter particle are currently determined from stacked analysis of all Milky Way satellite galaxies (e.g. McDaniel et al. 2024), again emphasizing the need for uniformly determined spectroscopic quantities. We leave a combined analyses based on this uniform DEIMOS sample to a future contribution.

6. SUMMARY

We present the largest self-consistent sample of spectroscopically-derived quantities for Milky Way satellite galaxies and globular clusters. The sample is based on a homogeneous re-analysis of stars observed with the Keck/DEIMOS spectrograph (Paper I, Geha et al. 2026). We determine uniform internal velocity dispersions, enclosed dynamical masses, mean [Fe/H] metallicities and internal metallicity spreads ($\sigma_{[\text{Fe}/\text{H}]}$) for systems with 10 or more member stars, and examine various scaling relations for these populations.

Previous population studies of the Milky Way’s stellar satellites have largely, and necessarily, relied on heterogeneous datasets when examining spectroscopic-based properties. While in many cases our results agree with the literature, our uniform analysis reduces the possibility of systematics due to aggregated data compilations. In summary, we find:

- At a given stellar mass, systems classified as satellite galaxies are well separated from globular clusters in their dynamical mass and mass-to-light ratios.
- For satellite galaxies, mass-to-light ratio increases with decreasing stellar mass. The maximum observed value is $M_{1/2}/L_{1/2} \sim 2500 \pm 1200$ for Segue 1 ($\log M_\star/M_\odot = 2.75$).
- For globular clusters, the enclosed stellar density ($\bar{\rho}_{1/2}$) is largest for globular clusters with small orbital pericenters and large stellar masses, consistent with dynamical processes acting on the Galactic globular cluster population.
- For globular clusters, we recover the known metallicity ‘floor’, with no observed clusters below $[\text{Fe}/\text{H}] < -2.4$.
- For satellite galaxies, the stellar-mass metallicity relationship is similar to previous work, but with a slightly steeper slope: $[\text{Fe}/\text{H}] = 0.33^{+0.04}_{-0.04} \log[M_\star] - 3.98^{+0.22}_{-0.21}$. The rms scatter around this relationship is 0.16 dex.
- For satellite galaxies below $\log M_\star/M_\odot \approx 4$, the mass-metallicity relation flattens and/or increases in scatter.
- Satellite galaxies have internal metallicity scatter that is constant between 0.3-0.4 dex across a wide range of stellar mass.
- For satellite galaxies, the distribution of σ_v vs. $r_{1/2}$ and $\bar{\rho}_{1/2}$ vs. $\log M_\star$ is consistent with CDM predictions, with a handful of outliers explained by tidal disruption.

- We provide measured quantities for all 67 systems presented in this work. This includes velocity dispersions, enclosed dynamical masses, $[\text{Fe}/\text{H}]$, $\sigma_{[\text{Fe}/\text{H}]}$, and associated errors (Table A1).

Due to proximity, the Milky Way’s population of satellite galaxies and star clusters includes, and will continue to include, the lowest mass and least chemically enriched stellar systems in the known Universe. The number of satellites, particularly at the faintest luminosities, is expected to increase dramatically with highly anticipated upcoming wide-field imaging surveys including LSST (Ivezić et al. 2019), the Roman Space Telescope (Spergel et al. 2015) and Euclid mission (Euclid Collaboration et al. 2025).

Our work highlights the importance of homogeneous spectroscopic follow-up of individual stars and a uniform analysis of properties in both known and anticipated low mass stellar systems around the Milky Way and beyond. In a future contribution, we will present a uniform analysis of Keck/DEIMOS archival data of M31 satellites, and work towards homogeneously merging other existing spectroscopic datasets (e.g., Tsantaki et al. 2022). Careful analysis of current spectroscopic datasets can provide key first-epoch spectroscopic measurements for current and future highly multiplexed spectroscopic surveys targeting individual stars in Milky Way satellites such as DESI (Cooper et al. 2023), PFS (Hirai et al. 2024), 4MOST (Skúladóttir et al. 2023), and the *Via Project*. Such work will ultimately enable tighter constraints on the low mass stellar mass-halo mass relation, im-

proved J-factor estimates for dark matter searches, and lay a foundation for interpreting the flood of new Milky Way satellites expected in the LSST/Roman era.

ACKNOWLEDGMENTS

MG was supported in part by a grant from the Howard Hughes Medical Institute (HHMI) through the HHMI Professors Program. We thank Yasmeen Asali, William Cerny, Vedant Chandra, Ivan Esteban, Erin Kado-Fong, Pratik Gandhi, Viraj Manwadkar, Sebastian Monzon, Ethan Nadler, Annika Peter, Frank van den Bosch and Risa Wechsler for insightful comments that improved this work. This work has made use of the Local Volume Database (Pace 2025). This research has made extensive use of the Keck Observatory Archive (KOA), which is operated by the W. M. Keck Observatory and the NASA Exoplanet Science Institute (NExSci), under contract with the National Aeronautics and Space Administration.

Software: This research made use of many community-developed or community-maintained software packages, including (in alphabetical order): Astropy (Astropy Collaboration et al. 2013), galpy (Bovy 2014) IPython (Perez & Granger 2007), Matplotlib (Hunter 2007), NumPy (van der Walt et al. 2011), Emcee (Foreman-Mackey et al. 2013), and SciPy (Jones et al. 2001). This research has also made use of NASA’s Astrophysics Data System.

Facility: Keck: DEIMOS

REFERENCES

Abdo, A. A., Ackermann, M., Ajello, M., et al. 2010, *ApJ*, 712, 147

Adelman-McCarthy, J. K., Agüeros, M. A., Allam, S. S., et al. 2008, *ApJS*, 175, 297

Agertz, O., Pontzen, A., Read, J. I., et al. 2020, *MNRAS*, 491, 1656

Ahvazi, N., Pace, A. B., Garling, C. T., et al. 2025, *arXiv e-prints*, arXiv:2511.15808

Alarcón Jara, A. G., Fellhauer, M., Simon, J., et al. 2023, *A&A*, 672, A131

Andersson, E. P., Rey, M. P., Yates, R. M., et al. 2025, *arXiv e-prints*, arXiv:2511.05695

Astropy Collaboration, Robitaille, T. P., Tollerud, E. J., et al. 2013, *A&A*, 558, A33

Bañares-Hernández, A., Read, J. I., & Júlio, M. P. 2025, *arXiv e-prints*, arXiv:2509.24103

Bailin, J. 2019, *ApJS*, 245, 5

Bastian, N., & Lardo, C. 2018, *ARA&A*, 56, 83

Battaglia, G., Helmi, A., & Breddels, M. 2013, *NewAR*, 57, 52

Battaglia, G., Helmi, A., Tolstoy, E., et al. 2008, *ApJL*, 681, L13

Battaglia, G., & Nipoti, C. 2022, *Nature Astronomy*, 6, 659

Baumgardt, H., Faller, J., Meinhold, N., McGovern-Greco, C., & Hilker, M. 2022, *MNRAS*, 510, 3531

Baumgardt, H., & Hilker, M. 2018, *MNRAS*, 478, 1520

Baumgardt, H., Hilker, M., Sollima, A., & Bellini, A. 2019, *MNRAS*, 482, 5138

Bose, S., & Deason, A. J. 2025, *arXiv e-prints*, arXiv:2509.07066

Bovy, J. 2014, galpy: Galactic dynamics package, *Astrophysics Source Code Library*, record ascl:1411.008, ascl:1411.008

—. 2015, *ApJS*, 216, 29

Brown, S. T., Fattahi, A., Gutcke, T. A., et al. 2025, *arXiv e-prints*, arXiv:2511.21824

Bullock, J. S., & Boylan-Kolchin, M. 2017, *ARA&A*, 55, 343

Buttry, R., Pace, A. B., Koposov, S. E., et al. 2022, *MNRAS*, 514, 1706

Carlin, J. L., & Sand, D. J. 2018, *ApJ*, 865, 7

Carrera, R., Pancino, E., Gallart, C., & del Pino, A. 2013, *MNRAS*, 434, 1681

Carretta, E., Bragaglia, A., Gratton, R., D’Orazi, V., & Lucatello, S. 2009, [A&A](#), **508**, 695

Cerny, W., Chiti, A., Geha, M., et al. 2025a, [ApJ](#), **979**, 164

Cerny, W., Bissonette, D., Ji, A. P., et al. 2025b, [arXiv e-prints](#), [arXiv:2510.02431](#)

Cohen, J. G., Kirby, E. N., Simon, J. D., & Geha, M. 2010, [ApJ](#), **725**, 288

Collins, M. L. M., Tollerud, E. J., Sand, D. J., et al. 2017, [MNRAS](#), **467**, 573

Conroy, C., & Gunn, J. E. 2010, FSPS: Flexible Stellar Population Synthesis, [Astrophysics Source Code Library](#), record ascl:1010.043, [ascl:1010.043](#)

Cooper, A. P., Koposov, S. E., Allende Prieto, C., et al. 2023, [ApJ](#), **947**, 37

Cruz, A., Brooks, A., Lisanti, M., et al. 2025, [arXiv e-prints](#), [arXiv:2510.11800](#)

Danieli, S., Greene, J. E., Carlsten, S., et al. 2023, [ApJ](#), **956**, 6

Delos, M. S., Ahvazi, N., & Benson, A. 2025, [arXiv e-prints](#), [arXiv:2512.04156](#)

Errani, R., Ibata, R., Navarro, J. F., Peñarrubia, J., & Walker, M. G. 2024, [ApJ](#), **968**, 89

Errani, R., Navarro, J. F., Ibata, R., & Peñarrubia, J. 2022, [MNRAS](#), **511**, 6001

Escala, I., Wetzel, A., Kirby, E. N., et al. 2018, [MNRAS](#), **474**, 2194

Esteban, I., Peter, A. H. G., & Kim, S. Y. 2024, [PhRvD](#), **110**, 123013

Euclid Collaboration, Mellier, Y., Abdurro’uf, et al. 2025, [A&A](#), **697**, A1

Faber, S. M., et al. 2003, in *Instrument Design and Performance for Optical/Infrared Ground-based Telescopes*. Edited by Iye & Moorwood, [Proceedings of the SPIE](#), Volume 4841, pp. 1657

Foreman-Mackey, D., Hogg, D. W., Lang, D., & Goodman, J. 2013, [PASP](#), **125**, 306

Fu, S. W., Weisz, D. R., Starkenburg, E., et al. 2023, [ApJ](#), **958**, 167

Gaia Collaboration, Vallenari, A., Brown, A. G. A., et al. 2023, [A&A](#), **674**, A1

Gallazzi, A., Charlot, S., Brinchmann, J., White, S. D. M., & Tremonti, C. A. 2005, [MNRAS](#), **362**, 41

Gandhi, P. J., Wetzel, A., Hopkins, P. F., et al. 2022, [MNRAS](#), **516**, 1941

Geha, M., Willman, B., Simon, J. D., et al. 2009, [ApJ](#), **692**, 1464

Geha, M., Pelliccia, D., Prochaska, J. X., et al. 2026, [ApJ](#), <https://doi.org/10.3847/1538-4357/abf333>

Gnedin, O. Y., & Ostriker, J. P. 1997, [ApJ](#), **474**, 223

Go, M., Jeon, M., Choi, Y., et al. 2025, [ApJ](#), **986**, 214

Gration, A., Hendriks, D. D., Das, P., Heber, D., & Izzard, R. G. 2025, [MNRAS](#), **543**, 1120

Guerra, J., Geha, M., & Strigari, L. E. 2023, [ApJ](#), **943**, 121

Harris, W. E. 2010, [arXiv e-prints](#), [arXiv:1012.3224](#) [astro-ph.GA]

Heiger, M. E., Li, T. S., Pace, A. B., et al. 2024, [ApJ](#), **961**, 234

Helmi, A., Irwin, M. J., Tolstoy, E., et al. 2006, [ApJL](#), **651**, L121

Hirai, Y., Kirby, E. N., Chiba, M., et al. 2024, [ApJ](#), **970**, 105

Hunter, J. D. 2007, [Computing in Science Engineering](#), **9**, 90

Ivezić, Ž., Kahn, S. M., Tyson, J. A., et al. 2019, [ApJ](#), **873**, 111

Jones, E., Oliphant, T., Peterson, P., et al. 2001, SciPy: Open source scientific tools for Python, [Online; [scipy.org](#)]

Kaplinghat, M., Valli, M., & Yu, H.-B. 2019, [MNRAS](#), **490**, 231

Kass, R. E., & Raftery, A. E. 1995, [Journal of the American Statistical Association](#), **90**, 773

Kim, D., Jerjen, H., Geha, M., et al. 2016, [ApJ](#), **833**, 16

Kirby, E. N., Cohen, J. G., Guhathakurta, P., et al. 2013, [ApJ](#), **779**, 102

Kirby, E. N., Cohen, J. G., Smith, G. H., et al. 2011, [ApJ](#), **727**, 79

Kirby, E. N., Guhathakurta, P., Simon, J. D., et al. 2010, [ApJS](#), **191**, 352

Koposov, S. E., Li, T. S., Allende Prieto, C., et al. 2025, [arXiv e-prints](#), [arXiv:2505.14787](#)

Kravtsov, A., & Wu, Z. 2023, [MNRAS](#), **525**, 325

Kravtsov, A. V. 2013, [ApJL](#), **764**, L31

Larsen, S. S., Baumgardt, H., Bastian, N., Hernandez, S., & Brodie, J. 2019, [A&A](#), **624**, A25

Latour, M., Kamann, S., Martocchia, S., et al. 2025, [A&A](#), **694**, A248

Leitinger, E. I., Baumgardt, H., Cabrera-Ziri, I., et al. 2025, [A&A](#), **694**, A184

Li, T. S., Koposov, S. E., Zucker, D. B., et al. 2019, [MNRAS](#), **490**, 3508

Longeard, N., Martin, N., Starkenburg, E., et al. 2020, [MNRAS](#), **491**, 356

Longeard, N., Martin, N., Ibata, R. A., et al. 2021, [MNRAS](#), **503**, 2754

Macciò, A. V., Frings, J., Buck, T., et al. 2017, [MNRAS](#), **472**, 2356

Majewski, S. R., Skrutskie, M. F., Weinberg, M. D., & Ostheimer, J. C. 2003, [ApJ](#), **599**, 1082

Majewski, S. R., Schiavon, R. P., Frinchaboy, P. M., et al. 2017, [AJ](#), **154**, 94

Manwadkar, V., & Kravtsov, A. V. 2022, [MNRAS](#), **516**, 3944

Martin, N. F., Ibata, R. A., Chapman, S. C., Irwin, M., & Lewis, G. F. 2007, [MNRAS](#), **380**, 281

May, S., Dalal, N., & Kravtsov, A. 2025, [arXiv e-prints](#), [arXiv:2509.02781](#)

McDaniel, A., Ajello, M., Karwin, C. M., et al. 2024, [PhRvD](#), **109**, 063024

Minor, Q. E., Pace, A. B., Marshall, J. L., & Strigari, L. E. 2019, [MNRAS](#), **487**, 2961

Munshi, F., Brooks, A. M., Applebaum, E., et al. 2021, [ApJ](#), **923**, 35

Nadler, E. O. 2025, [ApJL](#), **983**, L23

Nadler, E. O., Gluscevic, V., Driskell, T., et al. 2024, [ApJ](#), **967**, 61

Nadler, E. O., Wechsler, R. H., Bechtol, K., et al. 2020, *ApJ*, 893, 48

Navabi, M., Carrera, R., Noël, N. E. D., et al. 2026, *MNRAS*, 546, stag019

Ou, X., Chiti, A., Shipp, N., et al. 2024, *ApJ*, 966, 33

Pace, A. B. 2025, *The Open Journal of Astrophysics*, 8, 142

Pace, A. B., Erkal, D., & Li, T. S. 2022, *ApJ*, 940, 136

Pace, A. B., & Strigari, L. E. 2019, *MNRAS*, 482, 3480

Pace, A. B., Kaplinghat, M., Kirby, E., et al. 2020, *MNRAS*, 495, 3022

Pace, A. B., Koposov, S. E., Walker, M. G., et al. 2023, *MNRAS*, 526, 1075

Pace, A. B., Li, T. S., Ji, A. P., et al. 2025, *The Open Journal of Astrophysics*, 8, 112

Perez, F., & Granger, B. E. 2007, *Computing in Science Engineering*, 9, 21

Pianta, C., Capuzzo-Dolcetta, R., & Carraro, G. 2022, *ApJ*, 939, 3

Prochaska, J., Hennawi, J., Westfall, K., et al. 2020, *The Journal of Open Source Software*, 5, 2308

Read, J. I., Mamon, G. A., Vasiliev, E., et al. 2021, *MNRAS*, 501, 978

Rey, M. P., Taylor, E., Gray, E. I., et al. 2025a, *MNRAS*, 541, 1195

Rey, M. P., Katz, H., Cadiou, C., et al. 2025b, *arXiv e-prints*, arXiv:2510.05232

Riley, A. H., Bieri, R., Deason, A. J., et al. 2025, *arXiv e-prints*, arXiv:2509.06859

Sales, L. V., Wetzel, A., & Fattah, A. 2022, *Nature Astronomy*, 6, 897

Sandford, N. R., Li, T. S., Koposov, S. E., et al. 2025, *arXiv e-prints*, arXiv:2509.02546

Simon, J. D. 2019, *ARA&A*, 57, 375

Simon, J. D., & Geha, M. 2007, *ApJ*, 670, 313

Simon, J. D., Li, T. S., Ji, A. P., et al. 2024, *ApJ*, 976, 256

Skúladóttir, Á., Puls, A. A., Amarsi, A. M., et al. 2023, *The Messenger*, 190, 19

Smith, S. E. T., Cerny, W., Hayes, C. R., et al. 2024, *ApJ*, 961, 92

Sollima, A., Baumgardt, H., & Hilker, M. 2019, *MNRAS*, 485, 1460

Speagle, J. S. 2020, *MNRAS*, 493, 3132

Spergel, D., Gehrels, N., Baltay, C., et al. 2015, *arXiv e-prints*, arXiv:1503.03757

Strigari, L. E. 2018, *Reports on Progress in Physics*, 81, 056901

Strigari, L. E., Bullock, J. S., Kaplinghat, M., et al. 2008, *Nature*, 454, 1096

Tan, C. Y., Cerny, W., Drlica-Wagner, A., et al. 2025, *ApJ*, 979, 176

Taylor, E. D., Read, J. I., Orkney, M. D. A., et al. 2025, *Nature*, 645, 327

Tolstoy, E., Skúladóttir, Á., Battaglia, G., et al. 2023, *A&A*, 675, 49

Tsantaki, M., Pancino, E., Marrese, P., et al. 2022, *A&A*, 659, A95

Usman, S. A., Ji, A. P., Rodriguez, J., et al. 2025, *The Open Journal of Astrophysics*, 8, 86

van der Walt, S., Colbert, S. C., & Varoquaux, G. 2011, *Computing in Science Engineering*, 13, 22

Walker, M. G., Caldwell, N., Mateo, M., et al. 2023, *ApJS*, 268, 19

Walker, M. G., Mateo, M., Olszewski, E. W., et al. 2006, *AJ*, 131, 2114

—. 2007, *ApJL*, 667, L53

Wetzel, A. R., Hopkins, P. F., Kim, J.-h., et al. 2016, *ApJL*, 827, L23

Wheeler, C., Hopkins, P. F., Pace, A. B., et al. 2019, *MNRAS*, 490, 4447

Wheeler, C., Moreno, J., Rodriguez Wimberly, M. K., et al. 2025a, *arXiv e-prints*, arXiv:2506.15785

Wheeler, V., Kravtsov, A., Chiti, A., Katz, H., & Semenov, V. A. 2025b, *The Open Journal of Astrophysics*, 8, 151

Willman, B., Geha, M., Strader, J., et al. 2011, *AJ*, 142, 128

Willman, B., & Strader, J. 2012, *AJ*, 144, 76

Wolf, J., Martinez, G. D., Bullock, J. S., et al. 2010, *MNRAS*, 406, 1220

Xiang, M., Ting, Y.-S., Rix, H.-W., et al. 2019, *ApJS*, 245, 34

Yang, H., Wang, W., Zhu, L., et al. 2025, *ApJ*, 993, 249

Zaremba, D., Venn, K., Hayes, C. R., et al. 2025, *ApJ*, 987, 217

Zonoozi, A. H., Küpper, A. H. W., Baumgardt, H., et al. 2011, *MNRAS*, 411, 1989

Zonoozi, A. H., Rabiee, M., Hagh, H., & Kroupa, P. 2024, *ApJ*, 975, 266

APPENDIX

A. COMPARISON TO LITERATURE MEASUREMENTS

We compare our uniformly-determined DEIMOS-only measurements presented in this paper to the literature compilation v1.0.6 from [Pace \(2025\)](#). For this comparison, we focus only on systems identified as satellite galaxies. In the left panels of Figures [A1](#), [A2](#), and [A3](#), we plot our DEIMOS-determined measurements as red symbols, and a linear fit to these data as a red line.

In the right panels of Figures [A1](#)–[A3](#), blue symbols are literature values for the same satellite systems included in the DEIMOS sample. In some cases, these are based on the same DEIMOS dataset, but different data reduction pipelines. The DEIMOS sample itself is complete for currently known satellite galaxies with Declination $> -40^\circ$, with the exception of Antlia II and Crater II. There are 12 known satellite galaxies which are not in the DEIMOS archives, shown as green symbols in Figures [A1](#)–[A3](#). In these figures, the blue line is a fit to the blue sample, while the green line is a fit to the combined blue and green literature samples. For direct comparison, we repeat the red line determined from DEIMOS-only measurements in the both panels.

In the left panels of Figures [A1](#)–[A3](#), we also compare to selected literature predictions. This is not intended as a comprehensive comparison, but instead plot recent published predictions which can be directly compared. From the semi-analytic model GRUMPY, we plot the predicted enclosed dynamical mass from [Kravtsov & Wu \(2023\)](#) in Figure [A1](#) and the predicted stellar mass-metallicity relation from [Manwadkar & Kravtsov \(2022\)](#) in Figure [A2](#). From the semi-analytic model Galacticus ([Ahvazi et al. 2025](#)), we plot the predicted velocity dispersion versus stellar mass in Figure [6](#), and the stellar mass-metallicity relation in Figure [A2](#).

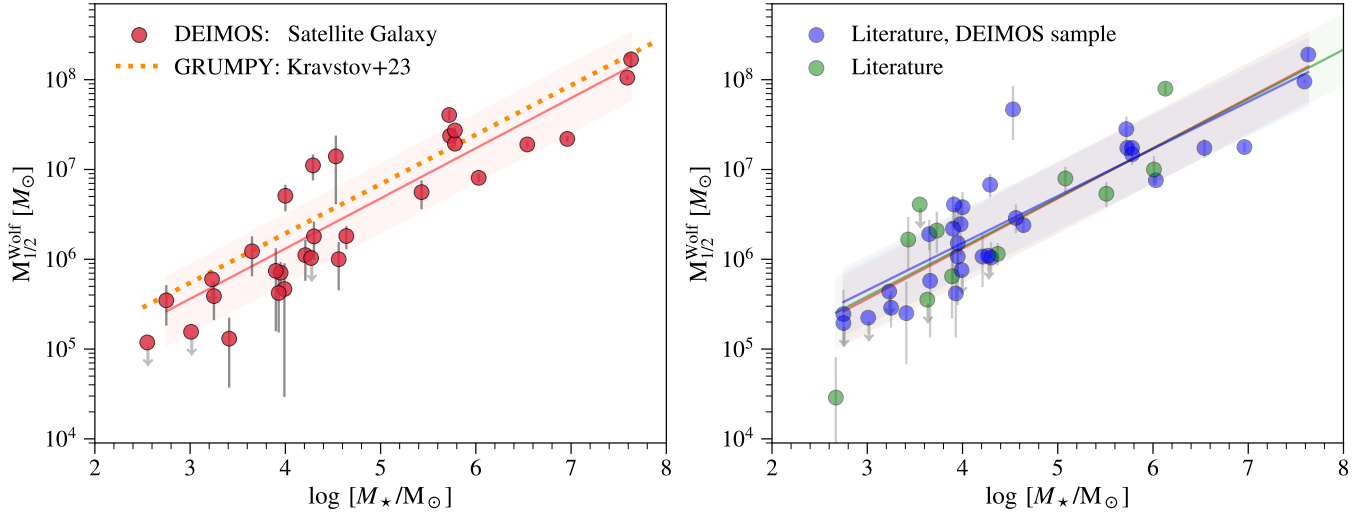


Figure A1. Focusing only on satellite galaxies, we plot the enclosed dynamical mass versus stellar mass, $M_{1/2}$ vs. $\log M_{\star}$. *Left:* We include the uniform measurements from the DEIMOS-only sample presented in this paper (red symbols) and fit a linear function (red line). We also include a comparison to the GRUMPY semi-analytic model (orange dotted line Kravtsov & Wu 2023). *Right:* Literature values taken from v1.0.6 of Pace (2025). Blue symbols are literature values for the same set of systems presented in the left panel, green are literature values for Milky Way satellites not covered by Keck/DEIMOS. The red line DEIMOS-only fit is repeated in both panels.

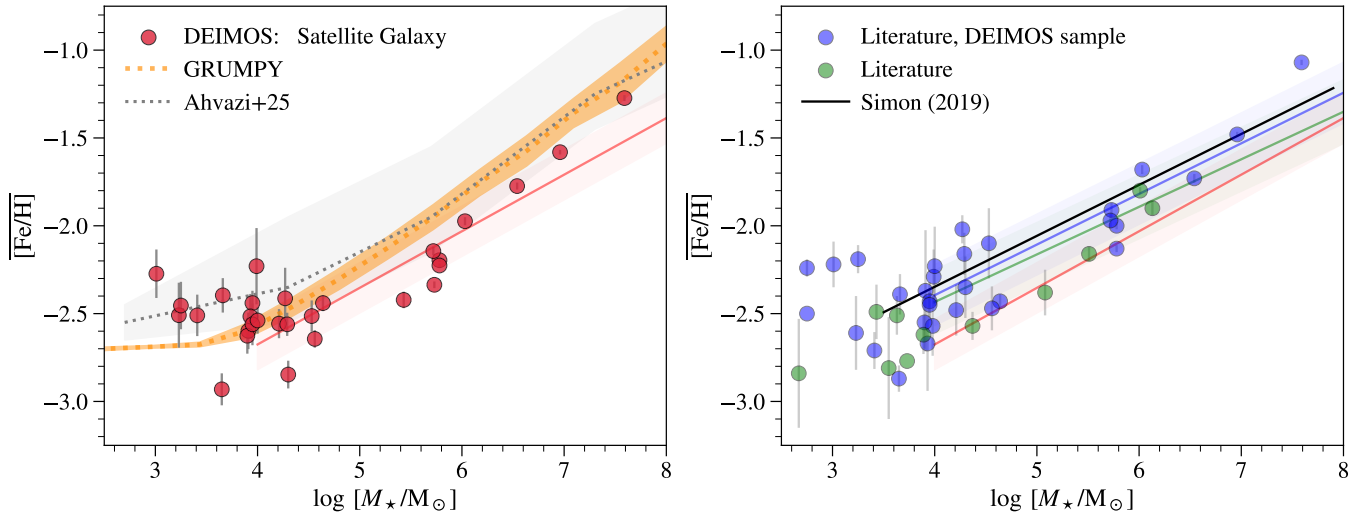


Figure A2. Focusing only on satellite galaxies, we plot the stellar metallicity versus stellar mass, $[\text{Fe}/\text{H}]$ vs. M_{\star} . Red/blue/green symbols are the same as Figure A1. *Left:* We compare to the semi-analytic predictions from GRUMPY (orange dotted Manwadkar & Kravtsov 2022) and Galacticus (gray dotted Ahvazi et al. 2025). Both models suggest a similar flattening below $\log M_{\star}/M_{\odot} \approx 4$ as observed. *Right:* In comparison to the Pace (2025) compilation, the DEIMOS-only stellar mass-metallicity relationship is slightly steeper and the normalization is 0.15 dex lower.

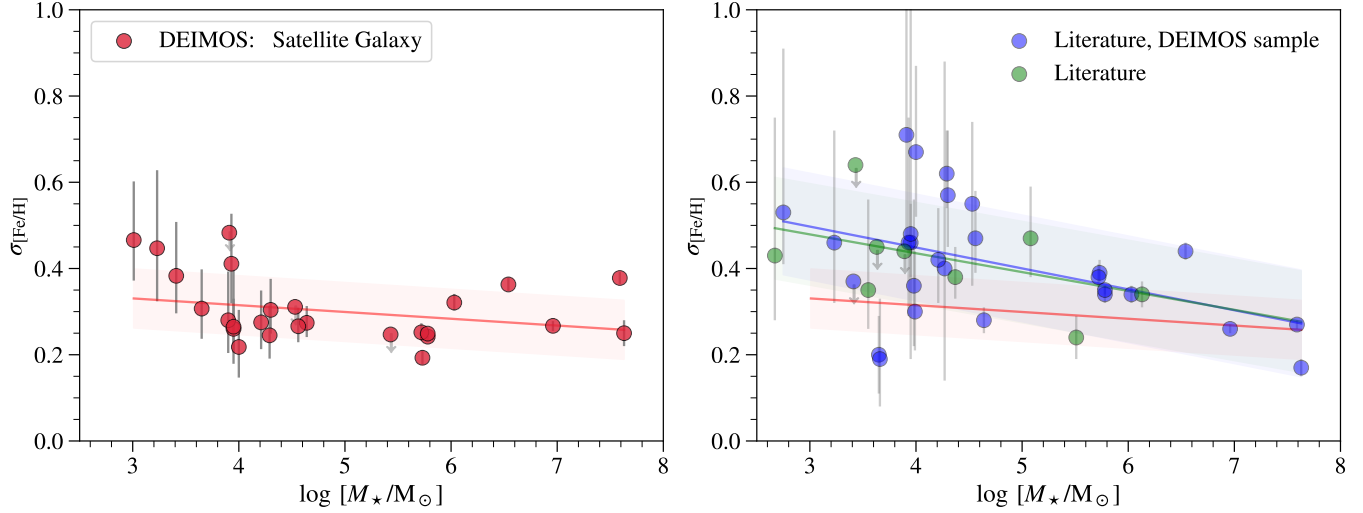


Figure A3. Focusing only on satellite galaxies, we plot the stellar metallicity dispersion versus stellar mass, $\sigma_{\text{[Fe/H]}}$ vs. M_\star . Red/blue/green symbols are the same as Figure A1. *Right:* In comparison to the Pace (2025) compilation, the DEIMOS-only stellar metallicity spreads are smaller and show less dependence on stellar mass.

Table A1. Derived Properties of Milky Way Satellites Observed with Keck/DEIMOS

Full Name	System Name	RA [deg]	Dec [deg]	Dist [kpc]	M_V [']	$r_{1/2}$ [']	Type	N_*	v_{sys} [km/s]	ϵ_{sys} [km/s]	$\sigma_{\text{sys}}^{2r_{\text{eff}}}$ [km/s]	$\epsilon_{\sigma_{\text{sys}}}^{ul}$	$\epsilon_{\sigma_{\text{sys}}}^{ll}$	$\overline{[\text{Fe}/\text{H}]}$	$\epsilon_{\sigma_{[\text{Fe}/\text{H}]}}^{ul}$	$\epsilon_{\sigma_{[\text{Fe}/\text{H}]}}^{ll}$	$\epsilon_{\sigma_{[\text{Fe}/\text{H}]}}^{ul}$	$\epsilon_{\sigma_{[\text{Fe}/\text{H}]}}^{ll}$		
(1)	(2)	(3)	(4)	(5)	(6)	(7)	(8)	(9)	(10)	(11)	(12)	(13)	(14)	(15)	(16)	(17)	(18)	(19)	(20)	(21)
Aquarius III	Aqr3	357.2200	-3.4900	85.5	-2.5	0.052	G	11	-13.2	1.0	-999	-999	3.65	-2.51	0.18	0.45	0.12	0.18	-999	
Bootes I	Boo1	210.0200	14.5135	66.4	-6.0	0.192	G	90	101.9	0.5	3.19	0.41	0.48	-999	-2.44	0.05	0.27	0.03	0.04	-999
Bootes II	Boo2	209.5141	12.8553	41.7	-2.9	0.038	G	17	-128.4	0.7	1.92	0.6	0.77	-999	-2.51	0.12	0.38	0.09	0.12	-999
Bootes III	Boo3	209.3000	26.8000	46.6	-5.7	0.548	G	16	189.9	1.8	5.27	1.67	2.1	-999	-2.51	0.09	-999	-999	-999	0.31
ComaBer	CB	186.7454	23.9069	42.3	-4.3	0.069	G	82	93.5	0.6	3.33	0.46	0.58	-999	-2.44	0.07	0.26	0.06	0.07	-999
CVn I	CVn1	202.0091	33.5521	210.9	-8.7	0.436	G	254	30.5	0.6	7.66	0.41	0.44	-999	-2.34	0.02	0.19	0.02	0.02	-999
CVn II	CVn2	194.2927	34.3226	160.0	-5.2	0.07	G	25	-131.8	1.2	5.28	0.96	1.25	-999	-2.85	0.08	0.30	0.05	0.07	-999
Draco	Dra	260.0685	57.9185	81.5	-8.9	0.229	G	995	-292.2	0.3	9.55	0.25	0.26	-999	-2.20	0.01	0.24	0.01	0.01	-999
Draco II	Dra2	238.2000	64.5700	21.6	-0.8	0.019	G	25	-342.3	0.7	-999	-999	2.64	-999	-999	-999	-999	-999	-999	0.23
Eridanus	Eri	66.1853	-21.1876	84.7	-5.4	0.016	GC	24	-18.4	0.3	-999	-999	0.89	-1.29	0.05	-999	-999	-999	-999	0.23
Eridanus 4	Eri4	76.4380	-9.5150	69.8	-3.5	0.065	G	19	-34.4	1.3	4.55	0.89	1.15	-999	-2.93	0.09	0.31	0.07	0.09	-999
Fornax	For	39.9583	-34.4997	142.6	-13.4	0.825	G	663	53.9	0.5	11.71	0.33	0.36	-999	-1.27	0.02	0.38	0.01	0.01	-999
Herc	Herc	247.7722	12.7852	130.6	-5.8	0.213	G	43	45.3	0.6	2.25	0.61	0.67	-999	-2.64	0.05	0.27	0.04	0.04	-999
Hydra 2	Hyd2	185.4251	-31.9860	151.4	-5.1	0.066	G	11	304.4	1.1	-999	-999	4.11	-2.41	0.17	-999	-999	-999	-999	0.25
Koposov 2	K2	119.5715	26.2574	24.0	-0.9	0.004	U	13	108.2	1.3	-999	-999	5.23	-999	-999	-999	-999	-999	-999	0.25
Leo I	Leo1	152.1146	12.3059	258.2	-11.8	0.274	G	686	285.9	0.4	9.29	0.26	0.26	-999	-1.58	0.01	0.27	0.01	0.01	-999
Leo II	Leo2	168.3627	22.1529	208.9	-9.5	0.153	G	253	78.8	0.5	7.53	0.36	0.39	-999	-1.97	0.02	0.32	0.02	0.02	-999
Leo IV	Leo4	173.2405	-0.5431	151.4	-5.0	0.111	G	24	129.8	0.9	3.29	0.66	0.89	-999	-2.56	0.08	0.28	0.06	0.07	-999
Leo V	Leo5	172.7857	2.2194	169.0	-4.4	0.049	G	10	170.8	1.5	3.37	1.04	1.72	-999	-2.23	0.22	-999	-999	-999	-999
Leo T	LeoT	143.7292	17.0482	413.1	-8.0	0.167	G	42	37.1	1.1	6.05	0.86	1.07	-999	-2.42	0.05	-999	-999	-999	0.25
NGC 1904	NGC1904	81.0496	-24.5247	13.1	-7.7	0.003	GC	61	206.0	0.7	5.22	0.51	0.57	-999	-1.59	0.01	-999	-999	-999	0.06
NGC 2419	NGC2419	114.5354	38.8819	88.5	-9.4	0.022	GC	86	-20.9	0.5	4.69	0.38	0.43	-999	-2.02	0.02	-999	-999	-999	0.12
NGC 0288	N288	13.1977	-26.5899	9.0	-6.8	0.006	GC	473	-43.2	0.2	3.47	0.16	0.17	-999	-1.23	0.01	-999	-999	-999	0.03
NGC 4590	NGC4590	189.8667	-26.7430	10.4	-7.2	0.004	GC	103	-93.6	0.4	3.31	0.25	0.28	-999	-2.33	0.01	-999	-999	-999	0.03
NGC 5024	NGC5024	198.2301	18.1691	18.5	-8.7	0.006	GC	33	-64.8	0.8	3.77	0.57	0.66	-999	-1.95	0.02	-999	-999	-999	0.07
NGC 5053	NGC5053	199.1124	17.6977	17.5	-6.3	0.012	GC	83	42.5	0.2	-999	-999	1.2	-2.34	0.02	-999	-999	-999	-999	0.07
NGC 5272	NGC5272	205.5468	28.3755	10.2	-8.7	0.003	GC	44	-147.0	0.7	3.85	0.46	0.53	-999	-1.54	0.02	0.08	0.02	0.02	-999
NGC 5634	NGC5634	217.4053	-5.9764	25.9	-7.7	0.005	GC	42	-18.3	0.6	3.40	0.4	0.47	-999	-1.80	0.01	-999	-999	-999	0.05
NGC 5897	NGC5897	229.3517	-21.0101	12.6	-7.3	0.008	GC	152	101.4	0.3	2.93	0.21	0.25	-999	-2.01	0.01	-999	-999	-999	0.04

Table A1 *continued*

Table A1 (continued)

Full Name	System Name	RA [deg]	Dec [deg]	Dist [kpc]	M_V	$r_{1/2}$ [']	Type	N_*	v_{sys} [km/s]	ϵ_{sys} [km/s]	$\sigma_{\text{sys}}^{2r_{\text{eff}}}$ [km/s]	$\epsilon_{\text{sys}}^{ll}$ [km/s]	$\epsilon_{\text{sys}}^{95}$ [km/s]	$\overline{[\text{Fe}/\text{H}]}$	$\epsilon_{[\text{Fe}/\text{H}]}^{ll}$ [dex]	$\sigma_{[\text{Fe}/\text{H}]}^{ll}$ [dex]	$\epsilon_{[\text{Fe}/\text{H}]}^{ul}$ [dex]	$\sigma_{[\text{Fe}/\text{H}]}^{ul}$ [dex]	$\epsilon_{[\text{Fe}/\text{H}]}^{95}$ [dex]	
(1)	(2)	(3)	(4)	(5)	(6)	(7)	(8)	(9)	(10)	(11)	(12)	(13)	(14)	(15)	(16)	(17)	(18)	(19)	(20)	(21)
NGC 5904	N5904	229.6406	2.0827	7.5	-8.5	0.004	GC	50	55.2	0.7	4.49	0.47	0.56	-999	-1.24	0.02	-999	-999	-999	0.04
NGC 6205	N6205	250.4235	36.4613	7.4	-8.6	0.003	GC	72	-245.8	0.7	5.74	0.49	0.6	-999	-1.50	0.01	-999	-999	-999	0.04
NGC 6218	N6218	251.8105	-1.9478	5.1	-7.0	0.003	GC	11	-40.6	0.8	-999	-999	3.3	-999	-1.20	0.04	-999	-999	-999	-999
NGC 6229	N6229	251.7452	47.5278	30.1	-8.1	0.004	GC	31	-139.1	0.6	2.38	0.45	0.59	-999	-1.46	0.05	-999	-999	-999	0.14
NGC 6254	N6254	254.2875	-4.0993	5.1	-7.8	0.003	GC	12	73.5	1.9	6.18	1.27	1.85	-999	-1.46	0.05	-999	-999	-999	-999
NGC 6341	N6341	259.2803	43.1365	8.5	-8.2	0.002	GC	110	-120.0	0.5	4.61	0.36	0.4	-999	-2.35	0.01	-999	-999	-999	0.09
NGC 6366	N6366	261.9347	-5.0766	3.4	-6.0	0.004	GC	21	-120.6	0.8	3.28	0.57	0.76	-999	-0.63	0.05	-999	-999	-999	0.14
NGC 6624	N6624	275.9190	-30.3613	8.0	-7.4	0.002	GC	69	55.4	0.4	3.29	0.31	0.36	-999	-0.67	0.02	-999	-999	-999	0.04
NGC 6656	N6656	279.1008	-23.9034	3.3	-8.6	0.003	GC	74	-146.3	0.9	7.05	0.62	0.69	-999	-1.61	0.02	-999	-999	-999	0.14
NGC 6715	N6715	283.7639	-30.4799	26.3	-10.0	0.004	GC	15	142.2	1.6	6.04	1.08	1.45	-999	-1.33	0.03	-999	-999	-999	0.13
NGC 6779	N6779	289.1479	30.1845	10.4	-7.7	0.003	GC	74	-133.6	0.6	4.70	0.41	0.48	-999	-1.93	0.02	-999	-999	-999	0.06
NGC 6838	N6838	298.4421	18.7784	4.0	-6.6	0.003	GC	17	-21.8	0.6	2.07	0.47	0.58	-999	-0.73	0.05	-999	-999	-999	0.13
NGC 6864	N6864	301.5202	-21.9222	20.5	-8.5	0.003	GC	36	-186.3	0.7	3.66	0.48	0.56	-999	-1.08	0.03	-999	-999	-999	0.14
NGC 7006	N7006	315.3722	16.1871	39.3	-7.5	0.004	GC	22	-383.1	0.8	3.25	0.55	0.69	-999	-1.47	0.02	-999	-999	-999	0.07
NGC 7078	N7078	322.4932	12.1668	10.7	-9.2	0.002	GC	246	-105.5	0.4	6.18	0.3	0.33	-999	-2.33	0.01	-999	-999	-999	0.05
NGC 7089	N7089	323.3626	-0.8233	11.7	-9.1	0.003	GC	200	-2.6	0.5	6.81	0.34	0.41	-999	-1.53	0.01	-999	-999	-999	0.04
NGC 7099	N7099	325.0918	-23.1791	8.5	-7.4	0.003	GC	146	-185.1	0.4	4.01	0.28	0.3	-999	-2.27	0.01	-999	-999	-999	0.05
NGC 7492	N7492	347.1102	-15.6108	24.4	-5.9	0.009	GC	21	-175.4	0.5	1.75	0.46	0.51	-999	-1.86	0.02	-999	-999	-999	0.08
Palomar 13	Pal13	346.6858	12.7712	23.5	-3.1	0.008	GC	57	26.0	0.3	-999	-999	1.52	-1.64	0.03	-999	-999	-999	0.09	
Palomar 14	Pal14	242.7544	14.9584	73.6	-5.3	0.029	GC	25	73.1	0.4	-999	-999	1.56	-1.50	0.06	0.21	0.06	0.06	-999	
Palomar 2	Pal2	71.5248	31.3817	26.2	-8.3	0.009	GC	15	-111.7	1.3	4.45	0.9	1.29	-999	-999	-999	-999	-999	-999	-999
Palomar 5	Pal5	229.0220	-0.1113	21.9	-4.9	0.02	GC	77	-57.7	0.6	3.21	0.69	0.71	-999	-999	-999	-999	-999	-999	-999
Sculpior	Scl	15.0183	-33.7186	84.0	-10.8	0.273	G	379	110.7	0.5	8.66	0.33	0.33	-999	-1.77	0.02	0.36	0.02	0.02	-999
Segue 1	Seg1	151.7504	16.0756	22.9	-1.3	0.024	G	53	203.1	0.9	3.97	0.86	0.97	-999	-999	-999	-999	-999	-999	-999
Segue 2	Seg2	34.8226	20.1625	36.5	-1.9	0.04	G	29	-41.2	0.4	-999	-999	2.06	-2.27	0.14	0.47	0.09	0.14	-999	
Segue 3	Seg3	320.3795	19.1178	16.9	-0.1	0.002	GC	17	-165.5	0.8	-999	-999	3.27	-999	-999	-999	-999	-999	-999	-999
Sextans	Sext	153.2628	-1.6133	85.9	-8.7	0.569	G	239	221.9	0.6	8.77	0.47	0.49	-999	-2.14	0.02	0.25	0.02	0.02	-999
Sgr	Sgr	284.0952	-30.5499	26.3	-13.5	2.608	G	60	142.7	1.1	8.31	0.74	0.86	-999	-0.35	0.03	0.16	0.03	0.03	-999

Table A1 *continued*

Table A1 (continued)

Full Name	System Name	RA [deg]	Dec [deg]	Dist [kpc]	M_V	$r_{1/2}$	Type	N_*	v_{sys}	ϵ_{sys}	$\sigma_{\text{sys}}^{2r_{\text{eff}}}$	$\epsilon_{\sigma_{\text{sys}}}^{ll}$	$\epsilon_{\sigma_{\text{sys}}}^{ul}$	$\epsilon_{\sigma_{\text{sys}}}^{ll}$	$\epsilon_{\sigma_{\text{sys}}}^{ul}$	$\overline{[\text{Fe}/\text{H}]}$	$\sigma_{[\text{Fe}/\text{H}]}$	$\epsilon_{[\text{Fe}/\text{H}]}^{ll}$	$\sigma_{[\text{Fe}/\text{H}]}^{ll}$	$\epsilon_{[\text{Fe}/\text{H}]}^{ul}$
(1)	(2)	(3)	(4)	(5)	(6)	(7)	(8)	(9)	(10)	(11)	(12)	(13)	(14)	(15)	(16)	(17)	(18)	(19)	(20)	(21)
Sgr 2	Sgr2	298.1700	-22.0700	64.0	-5.8	0.034	GC	28	-176.4	0.6	2.32	0.43	0.53	-999	-2.31	0.04	-999	-999	-999	0.17
Terzan 5	Ter5	267.0021	-24.7792	6.6	-9.1	0.002	GC	15	-85.4	2.7	10.27	1.74	2.45	-999	-999	-999	-999	-999	-999	-999
UMa 1	UMa1	158.7706	51.9480	97.3	-5.1	0.234	G	36	-58.5	1.4	7.16	1.04	1.21	-999	-2.56	0.07	0.24	0.05	0.07	-999
UMa 2	UMa2	132.8726	63.1335	34.7	-4.4	0.139	G	64	-118.0	1.1	6.30	0.95	1.06	-999	-2.54	0.07	0.22	0.07	0.09	-999
Ursa Minor	UMi	227.2420	67.2221	70.2	-8.9	0.373	G	827	-246.1	0.3	8.86	0.24	0.27	-999	-2.23	0.01	0.25	0.01	0.01	-999
Unions 1	UNI1	174.7080	31.0711	10.0	2.2	0.003	U	10	89.6	0.9	-999	-999	4.35	-999	-999	-999	-999	-999	-999	-999
Willman 1	W1	162.3436	51.0501	38.0	-2.5	0.027	G	47	-12.5	0.9	3.97	0.72	0.88	-999	-2.45	0.14	-999	-999	-999	-999

Note—Literature and computed properties of Milky Way stellar satellites included in this work. (1)-(2) Name and abbreviated name of system, (3)-(7) position, distance, absolute magnitude and half-light radius taken from [Pace \(2025\)](#). (9) number of member stars identified. (10)-(11) The systematic velocity and associated error determined for the system. (12)-(15) The velocity dispersion and associated error determined for the system. (16)-(17) The mean [Fe/H] and error determined for the system. (18)-(21) The internal [Fe/H] spread and error determined for the system. The full contents of this table (67 rows) is available in a machine-readable format.